Impact of Microcrack Generation and Surface Degradation on Nickel-rich Layered $Li[Ni_{0.9}Co_{0.05}Mn_{0.05}]O_2$ Cathode for Lithium-ion Batteries

Ho-Hyun Sun and Arumugam Manthiram*

Materials Science and Engineering Program and Texas Materials Institute, The University of Texas at Austin, Texas 78712, United States

ABSTRACT: To address the increasing demand for energy density, the Ni-rich layered $Ni_{0.90}Co_{0.05}Mn_{0.05}]O_2$ cathode has been synthesized and its electrochemical performance in lithium-ion cells has been benchmarked against a lower Ni-content $Li[Ni_{0.6}Co_{0.2}Mn_{0.2}]O_2$. $Li[Ni_{0.90}Co_{0.05}Mn_{0.05}]O_2$ delivers a high discharge capacity of 227 mA h g^{-1} compared to 189 mA h g^{-1} for $Li[Ni_{0.6}Co_{0.2}Mn_{0.2}]O_2$ when cycled up to a lower cutoff voltage of 4.3 V, making it an appealing candidate for electric vehicles. On increasing the charge cutoff voltage to 4.5 V, $Li[Ni_{0.90}Co_{0.05}Mn_{0.05}]O_2$ displays a capacity of 238 mA h g^{-1} compared to 208 mA h g^{-1} for $Li[Ni_{0.6}Co_{0.2}Mn_{0.2}]O_2$. Although $Li[Ni_{0.90}Co_{0.05}Mn_{0.05}]O_2$ suffers during cycling from the usual rapid capacity fade similar to $LiNiO_2$, 87% and 81% of the initial capacity could still be retained after 100 cycles even after cycling to a higher cutoff voltage of 4.3 and 4.5 V, respectively. A comparison of $Li[Ni_{0.90}Co_{0.05}Mn_{0.05}]O_2$ and $Li[Ni_{0.6}Co_{0.2}Mn_{0.2}]O_2$ reveals that the capacity fade of $Li[Ni_{0.90}Co_{0.05}Mn_{0.05}]O_2$ originates largely from the anisotropic volume change and subsequent microcrack propagation in the bulk and NiO-like rock salt impurity phase formation on the particle surface, which are exacerbated at 4.5 V. Future work with appropriate doping and surface modification could improve further the performance of $Li[Ni_{0.90}Co_{0.05}Mn_{0.05}]O_2$.

1. INTRODUCTION

With the introduction of the first layered transition-metal oxide $LiCoO_2$ as a cathode in the 1st generation lithium-ion batteries (LIBs) by Sony in 1991, LIBs have experienced a tremendous expansion in usage from small portable electronic devices to electric vehicles (EVs) to energy storage power grids. With a practical specific capacity of ~ 140 mA h g^{-1} at a cutoff voltage of 4.2 V vs. Li^0/Li^+,[1–3] $LiCoO_2$ was able to satisfy much of the requirements for portable electronics. However, due to the increasing demand for higher energy density, lower cost, and environmental compatibility, $LiNiO_2$ is drawing much attention as a promising alternative due to its higher capacity of > 200 mA h g^{-1}, lower cost, and environmental benignity compared to $LiCoO_2$. However, $LiNiO_2$ suffers from (i) difficulty in synthesizing stoichiometric $LiNiO_2$ due to the instability of Ni^{3+} during the high-temperature synthesis and the consequent cation mixing[4–7] arising from a similar size of Ni^{2+} (0.69 Å) and Li^+ (0.76 Å) ions, (ii) surface degradation by the generation of NiO impurity on the cathode surface[8–10] due to the chemical instability of the highly oxidized Ni^{4+}, especially at the highly delithiated state, (iii) concurrent oxygen release from the host structure,[8,10,11] and (iv) micro-crack propagation in the bulk caused by multiple phase transformations during Li^+ extraction/insertion.[12–14] The combination of these problems results in a steep decline in electrochemical performance and increasing safety concerns. These problems have been alleviated by substituting Ni with Co and Mn to give $Li[Ni_xCo_yMn_z]O_2$ (NCM xyz) or Co and Al to give $Li[Ni_xCo_yAl_z]O_2$ (NCA xyz). A typical example of this strategy is $Li[Ni_{1/3}Co_{1/3}Mn_{1/3}]O_2$, which exhibits excellent capacity retention and safety, resulting in its successful commercialization.[15,16]

However, such improvements stem with a sacrifice in the practical capacity (~ 160 mA h g^{-1}). Considering the push to increase the driving range to 300 miles in a single-charge as outlined by DOE,[17] the corresponding energy density requirement is 350 W h kg^{-1} at the cell level and 800 W h kg^{-1} (216 mA h g^{-1} at 3.7 V) at the cathode active material level.[18,19] In this regard, the layered nickel-rich materials $Li[Ni_{1-x-y}Co_xMn_y]O_2$ ($x + y \leq 0.4$) has garnered much attention as a promising candidate for electric vehicles. The cathode capacity increases with increasing Ni content, but at the expense of cycle life.[20] Another approach to increase the specific capacity is to increase the charge cutoff voltage,[21,22] but the extraction of more Li weakens the layered structure and accelerates material degradation.[23] At present, cathodes with a composition of $Li[Ni_{0.6}Co_{0.2}Mn_{0.2}]O_2$ (NCM 622) with a cutoff voltage of 4.3 V is beginning to be employed in commercial cells, but its practical capacity is limited to 160 mA h g^{-1}.

To achieve the energy density target, both the Ni content in the cathode and the cutoff voltage have to be brought up as much as possible. In this regard, $Li[Ni_{0.9}Co_{0.05}Mn_{0.05}]O_2$ (NCM 900505) is a promising candidate, capable of pushing the energy density closer to the 300 mile goal. Despite its potential in terms of capacity, NCM 900505 is still an underexplored cathode material unlike NCM 622, due to the difficulty in the synthesis and poor thermal characteristics and cycle life. To the best of our knowledge, there is only one report on the investigation of NCM 900505.[24] We present here a high-performance NCM 900505 with superior cycle and a systematic study and comparison of NCM 900505 and NCM 622 with two charge cutoff voltages: 4.3 and 4.5 V. Based on the results, we discuss the mechanisms causing the capacity fade from a structural, thermal, and chemical perspective to develop a better understanding of Ni-rich NCMs.

2. EXPERIMENTAL SECTION

Synthesis of $Li[Ni_{0.6}Co_{0.2}Mn_{0.2}]O_2$ and $Li[Ni_{0.9}Co_{0.05}Mn_{0.05}]O_2$. Spherical $Li[Ni_{0.6}Co_{0.2}Mn_{0.2}]O_2$ and $Li[Ni_{0.9}Co_{0.05}Mn_{0.05}]O_2$ precursors were synthesized via a co-precipitation method where $NiSO_4{\cdot}6H_2O$, $CoSO_4{\cdot}H_2O$, and $MnSO_4{\cdot}5H_2O$ were fed into a batch reactor. The resulting $[Ni_{0.6}Co_{0.2}Mn_{0.2}](OH)_2$ and $[Ni_{0.9}Co_{0.05}Mn_{0.05}](OH)_2$ were filtered, washed, dried at 110 °C overnight, mixed with $LiOH{\cdot}H_2O$ in a LiOH/metal hydroxide = 1.01 ratio, and calcinated at 850 °C for $Li[Ni_{0.6}Co_{0.2}Mn_{0.2}]O_2$ and 750 °C for $Li[Ni_{0.9}Co_{0.05}Mn_{0.05}]O_2$ for 12 h.

Electrochemical Characterization. The synthesized lithium metal oxides were mixed with Super-P carbon and polyvinylidene fluoride (PVdF) in a 90 : 5.5: 4.5 ratio in *N*-methyl-2-pyrrolidone. The resulting slurry was then coated onto an aluminum foil and vacuum dried and roll-pressed. The electrode was then assembled in a 2032 coin-type cell with lithium metal as the anode and 1.2 M $LiPF_6$ in ethylene carbonate-ethyl methyl carbonate (EC : EMC = 3 : 7, vol. %) with 1 wt. % vinylene carbonate (VC) as the electrolyte. The cells were cycled for 100 cycles from 2.7 to 4.3 V vs. Li^0/Li^+ with a constant current of 120 mA g^{-1}, equivalent to 0.5 C-rate, at 30 °C.

Analytical Characterization. Inductively coupled plasma (ICP, OPIMA 8300, Perkin Elmer) analysis was used to determine the molar compositions of the $Li[Ni_{0.6}Co_{0.2}Mn_{0.2}]O_2$ and $Li[Ni_{0.9}Co_{0.05}Mn_{0.05}]O_2$ samples. Powder X-ray diffraction (XRD) was performed with Cu Kα radiation from 2θ = 10° to 110° with a step size of 0.01 ° with a Rigaku Rint-2000diffractometer. The XRD data were analyzed with Rietveld refinement by the Fullprof program. In addition, scanning electron microscopy (SEM, JEOL JSM 6400) and transmission electron microscopy (TEM, JEOL 2010) were used to analyze the surface and morphologies of the cathode samples before and after cycling and after focused ion beam (FIB) cutting. Electrochemical impedance spectroscopy (EIS) data were collected by charging the cells to 4.3 V after the 1st, 25th, 50th, 75th, and 100th cycles in the frequency range of 1 MHz to 1 mHz with an amplitude of 10 mV with a BioLogic impedance analyzer. Electrolyte dissolution tests were carried out by storing the electrodes charged to 4.3 V in the electrolyte (1.2 M $LiPF_6$ in EC : EMC = 3 : 7, vol. % with 2 wt. % VC) at an elevated temperature of 55 °C for 10 and 20 days after which the electrolyte was analyzed with ICP. Time-of-flight – secondary ion mass spectroscopy (TOF-SIMS, ION-TOF) was used for depth profiling and chemical analysis. Depth profiling and high-resolution image were taken with a 500 eV Cs^+ ion beam with a sputtering rate of ~ 0.03 nm s^{-1} over a 100 × 100 μ m^2 area. All samples were rinsed with dimethyl carbonate and dried in an argon-filled glovebox.

Differential Scanning Calorimetery (DSC) Analysis. The cells for DSC cells were charged at a constant voltage up to 4.3 V and disassembled in an argon-filled glovebox. The cathode was extracted from the cell and washed with dimethyl carbonate and vacuum dried and then carefully scratched from Al foil to recover the cathode. Afterwards, 5 – 7 mg of the sample was placed in a steel sealed pan with a gold plated copper seal and placed in a Pyris 1 differential scanning calorimeter (NETZSCH, DSC 200 PC). The scanning rate was 5 °C min^{-1}.

3. RESULT AND DISCUSSION

Crystal Chemistry and Morphology. The morphologies of the as-prepared $Li[Ni_{1-2x}Co_xMn_x]O_2$ (x = 0.05, 0.2) cathodes were analyzed with SEM as seen in Figure 1a-d. The secondary particles of both cathodes have spherical morphologies with a uniform size distribution of 8 – 10 μm and are agglomerations of crystalline primary particles, characteristic of the co-precipitation method.[20,25–28] The NCM 622 primary particles are bulkier with 1 μm size while the NCM 900505 primary particles are elongated with sizes of 400 nm. The chemical compositions of the synthesized cathodes were determined by ICP and were $Li[Ni_{0.6}Co_{0.2}Mn_{0.2}]O_2$ and $Li[Ni_{0.90}Co_{0.05}Mn_{0.05}]O_2$ with tap densities of 2.40 and 2.28 g cm^{-3}, respectively. Rietveld refined powder XRD patterns of the as-prepared $Li[Ni_{1-2x}Co_xMn_x]O_2$ (x = 0.05, 0.2) in Figure 1e and f (and Table S1 and 2) indicate that the patterns of both the cathodes have the rhombohedral α-$NaFeO_2$ layered structure with the space group of $R\bar{3}m$. The calculated lattice parameters are a = 2.8683(1) Å and c = 14.2241(4) Å for NCM 622 and a = 2.8735(1) Å and c = 14.2049(3) Å for NCM 900505. The extent of cation mixing, ascertained by the Rietveld refinement, was determined to be 3.4 % in NCM 622 and a less severe 1.8 % in NCM 900505. Cation mixing is engendered by the similar radii of Ni^{2+} (0.69 Å) and Li^+ (0.76 Å).[9,19,29] In the case of NCM 900505, the severity of this phenomenon is alleviated because with increasing Ni content, the oxidation state of Ni is closer to Ni^{3+} (0.60 Å),

making cation mixing less probable. Also, due to the higher oxidation state of Ni^{3+}, the c-axis has also been reduced.

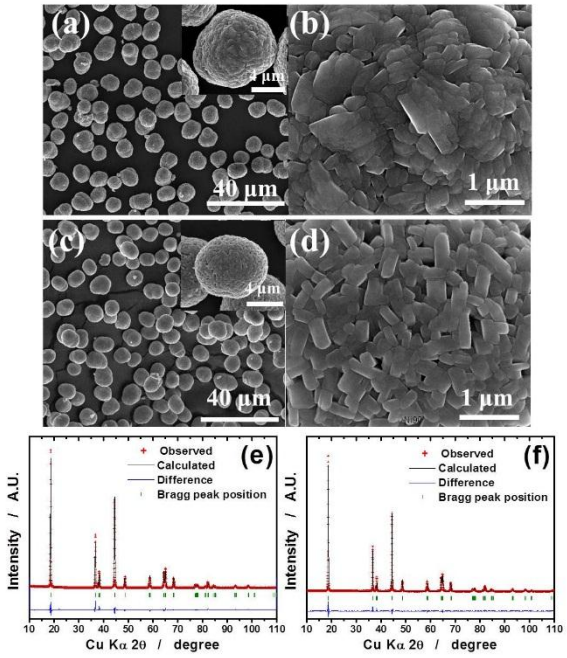

Figure 1. SEM images of (a-b) NCM 622 and (c-d) NCM 900505 cathode and Rietveld refinement of (e) NCM 622 and (f) NCM 900505.

Electrochemical Performance. The ramification of the increase in Ni content in $Li[Ni_{0.90}Co_{0.05}Mn_{0.05}]O_2$ compared to that in $Li[Ni_{0.60}Co_{0.2}Mn_{0.2}]O_2$ is much more evident in the electrochemical performances of the two cathode materials (Figure 2). Initial voltage profiles of NCM 622 and NCM 900505 (Figure 2a) are similar up to 3.7 V but diverge afterwards; whereas NCM 622 continues its voltage profile in a single plateau to deliver a discharge capacity of 188 mA h g^{-1}, NCM 900505 delivers a much higher discharge capacity of 227 mA h g^{-1} with two additional plateaus at 4.0 V and 4.18 V. At 4.5 V, the tails of the voltage profiles extend to give even higher discharge capacities of 208 mA h g^{-1} for the former and 238 mA h g^{-1} for the latter. This high capacity of NCM 900505 is derived from its high Ni content analogous to $LiNiO_2$, which delivered a practical capacity of 242 mA h g^{-1} at 4.3 V.[24] Thus, NCM 900505 is able to deliver a capacity that surpasses the 350 Wh Kg^{-1} energy density threshold on the cathode level suggested by DOE.[17] However, despite its outstanding capacity, NCM 900505 displays a rapid capacity fade similar to that observed with $LiNiO_2$[24] (Figure 2b); by the end of its 100th cycle, NCM 900505 retains only 87 % (182 mA h g^{-1}) of its original discharge capacity whereas

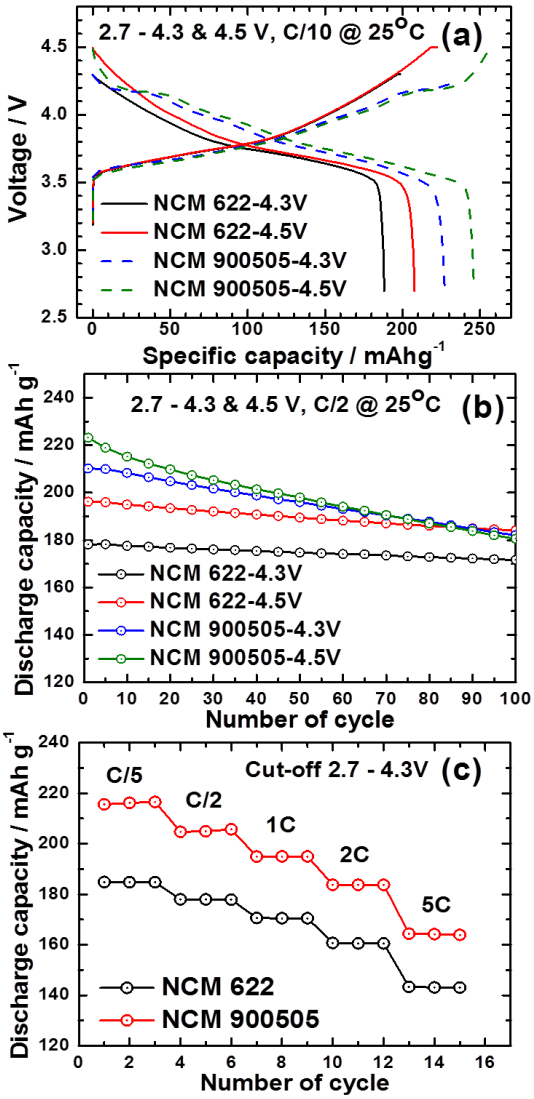

Figure 2. (a) Initial charge-discharge voltage profiles and (b) cycle life tests of NCM 622 and NCM 900505 cathodes in the voltage range of 2.7 – 4.3 V and 2. 7 – 4.5 V. (c) Rate capabilities of NCM 622 and NCM 900505 cathodes at various C rates from 0.2C to 5C-rate in the voltage range of 2.7 – 4.3 V.

NCM 622 retains 96 % (171 mA h g^{-1}) of its original capacity with a cutoff voltage of 4.3 V. At 4.5 V, this rapid capacity fade is exacerbated as the capacity retention of NCM 900505 further drops to 81 % compared to NCM 622(94 %).

Phase Transformation. The accelerated capacity fade of NCM 900505 is problematic as electric vehicle battery lifetime expectancy is 10+ years. To investigate the mechanism behind the rapid capacity fade of NCM 900505, redox peaks were correlated to the series of structural changes during cycling through dQ dV^{-1} profiles (Figure 3a-b). The dQ dV^{-1} profiles are in accordance with the previously reported literature.[19,23] In the discharged state, both profiles start at the rhombohedral phase (H1) and undergo structural transformation to monoclinic phase (M) phase at approximately 3.68

V. Beyond this redox peak, NCM 622 exhibits no further oxidation peaks, but NCM 900505 shows two more transformation redox peaks: one from M to the rhombohedral phase H2 and another from H2 to the rhombohedral phase H3. The gradual decrease in the H3 redox peak of NCM 900505 at 4.18 V with cycling is due to the reduction of the extent of H3 transformation. In contrast, the 50th and 100th profiles of NCM 622 remain almost identical to the 1st profile. Beyond 4.3 V, no other phase changes were observed for both NCM 622 and NCM 900505 (Figure S1).

To substantiate the extent of phase transformation incurred during charging, each cathode was charged to 4.1, 4.2, and 4.3 V and examined with *ex situ* XRD. The XRD data are shown in Figure S2 and the corresponding lattice parameter changes from refinement results are summarized in Figure 3c-d. In accordance with the dQ dV^{-1} profiles of the NCM 622 cathode showing no redox peaks beyond 4.1 V, the lattice parameters of NCM 622 hardly change during charging of the NCM 622 cathode above 4.1 V. On the other hand, NCM 900505 shows an abrupt contraction in the *c*-axis lattice parameter from 4.1 to 4.2 V due to the appearance of the H3 phase, which is similar to the behavior observed in the case of $LiNiO_2$.[29] The *c*-axis lattice contraction experienced by the NCM 900505 cathode amounts to ~ 4%, while *a*-axis lattice parameter remains nearly unchanged (0.2% contraction). Such an anisotropic lattice strain occurring repeatedly during cycling deteriorates the structural stability of the cathode; in the case of $LiNiO_2$, the lattice contraction was recently demonstrated to be the main cause of the capacity fading for the cathode[12] and also in the case of the $Li[Ni_{0.8}Co_{0.1}Mn_{0.1}]O_2$ cathode.[30] *Ex-situ* XRD patterns of NCM and corresponding lattice parameters before and after cycling are illustrated in Figure S3. While NCM 622 experiences minimal *c*-axis lattice parameter changes, NCM 900505 undergoes substantial *c*-axis parameter change from 14.195 to 14.209 Å at the end of its 100th cycle.

Microcrack Generation. To examine the effect of lattice parameter changes on the particle structure, a thin cross-section of a particle from the cycled NCM 900505 cathode at 4.3 V was prepared by FIB. Mosaic bright-field STEM image of the cycled NCM 900505 cathode (Figure 4a) shows that the microcracks, resulting from the detrimental lattice contraction/expansion arising from the H2 → H3 transition during cycling,[12] cause an interparticle crack network that compromise the primary particle connectivity. This separation of primary particles results in electrical contact loss and electrically isolated grains in the particle bulk as highlighted in the corresponding dark-field STEM image shown in Figure 4b. The separation width is ~ 5 nm as illustrated by the TEM image of the primary particles from the periphery (Figure 4c) and its high resolution TEM (HRTEM) image of the marked area (Figure 4d). The particle separation is also evident in the secondary particle interior (Figure 4e) in which clear interparticle microcracks are observed. A high-resolution image in Figure 4f from the marked region demonstrates

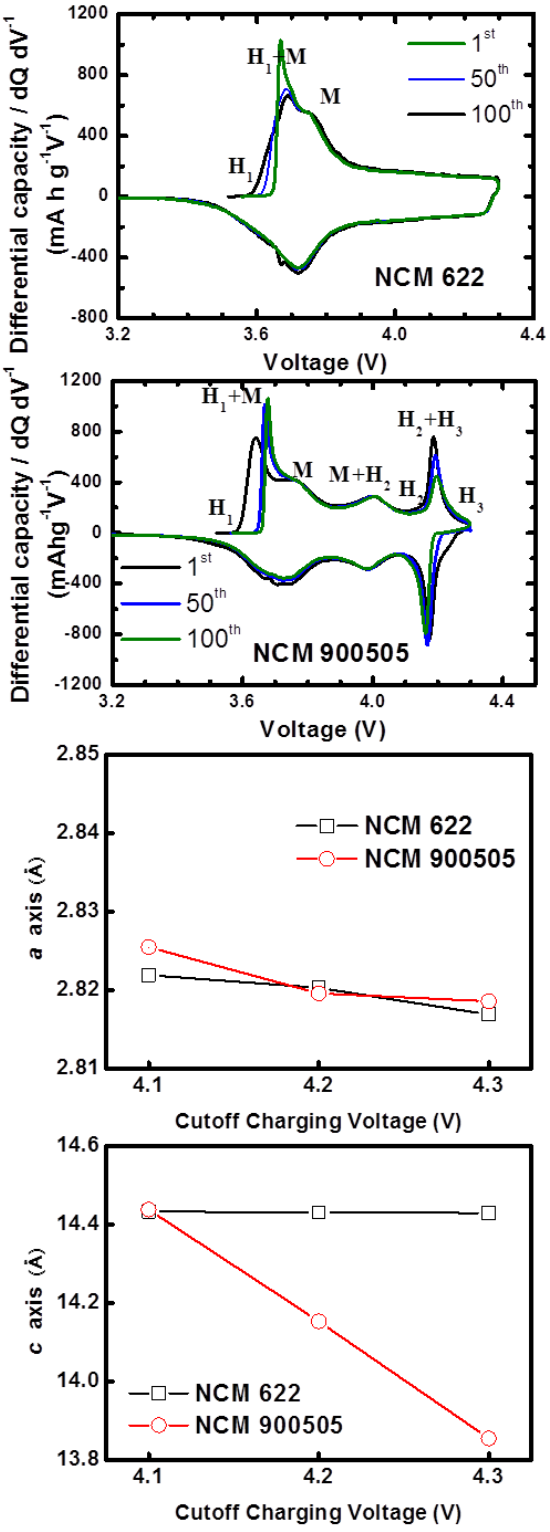

Figure 3. dQ dV^{-1} profiles of (a) NCM 622 and (b) NCM 900505 cathode in the voltage range of 2.7 – 4.3 V, and lattice parameter variations of NCM 622 and NCM 900505 cathodes with different charge cut-off voltages of 4.1 to 4.3 V at initial cycle: (c) *a*-axis and (d) *c*-axis.

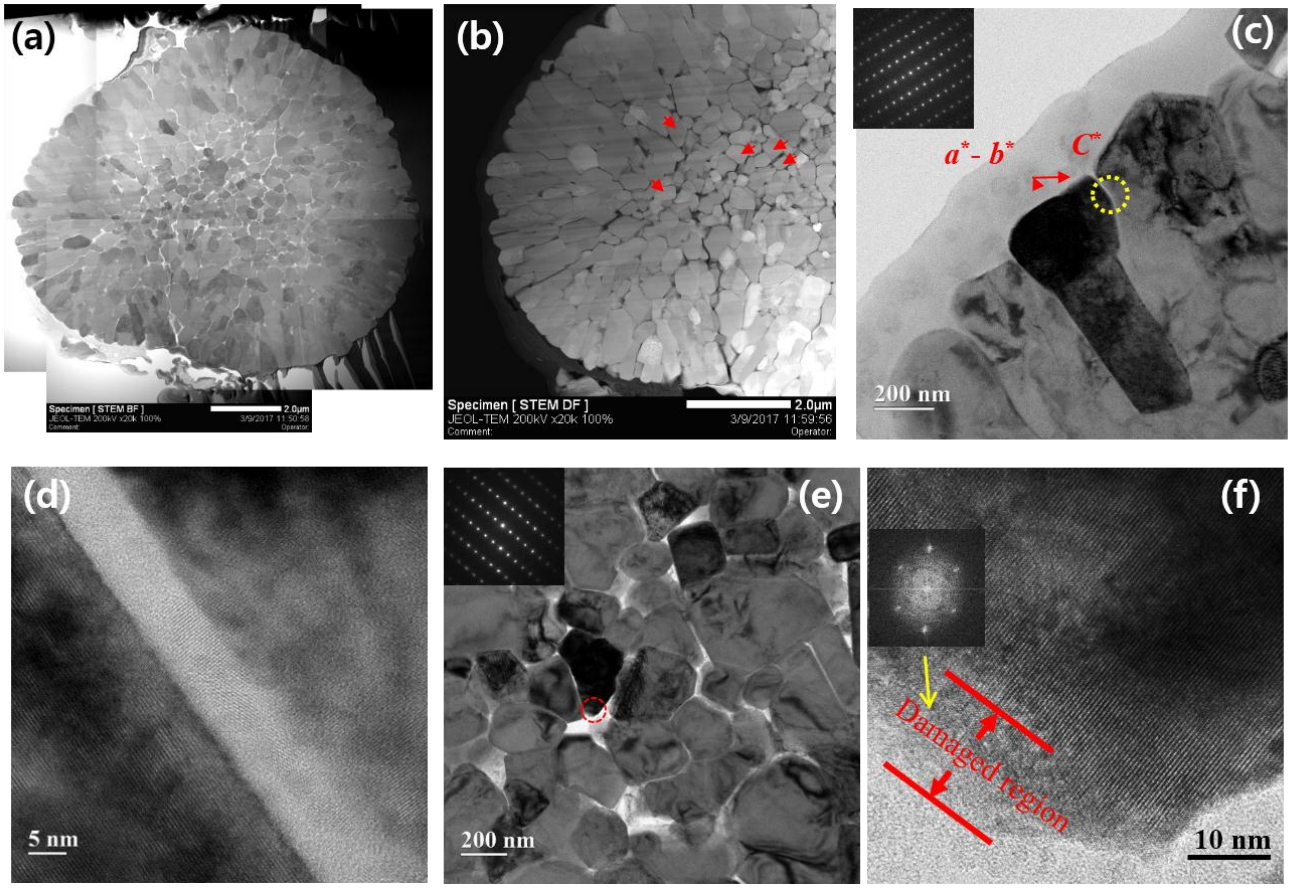

Figure 4. FIB-prepared NCM 900505 cathode charged after 100 cycles to 4.3 V: (a) mosaic bright-field STEM image, (b) dark-field STEM image, (c) conventional TEM image of the primary particles at the sample periphery showing grain separation, (d) HRTEM of the marked region in (c), (e) secondary particle interior TEM image, and (f) HRTEM of the marked region in (e) showing the primary particle surface degradation.

the surface damage incurred by the primary particle due to the electrolyte penetration through the secondary particle interior. These isolated grains in the bulk with high electrical resistance (from the NiO-like surface phase) further aggravates the charge transport, thus accelerating capacity fade of the NCM 900505. In fact, loss of primary particle connectivity and formation of NiO-like phase from microcracks have been attributed as the main degradation mechanism of $Li(Ni_{0.76}Co_{0.14}Al_{0.10})O_2$ and $Li(Ni_{0.8}Co_{0.15}Al_{0.05})O_2$. Raising the cutoff voltage to 4.5 V destroys further the mechanical integrity as evidenced by the nearly fractured NCM 900505 particle shown in Figure 5. At 4.5 V, the anisotropic strain is severe enough to even fracture the constituent primary particles as indicated by the red arrows in Figure 5b and c, which point out the internal cracks. In addition to the easily visible fracturing of the primary particles, structural damage also occurred at a microscopic scale as can be seen in Figure 5d, which shows a part (circled region) of a primary particle that is nearly broke off. The selected area electron diffraction from the area shown in the inset is a ring pattern,

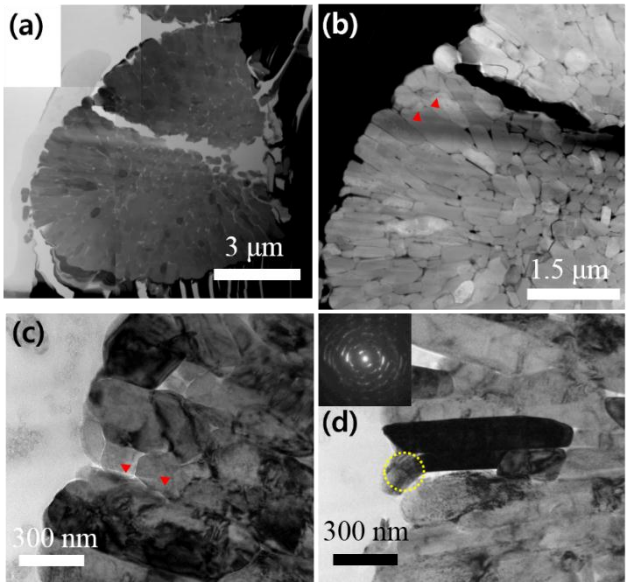

Figure 5. TEM images of the FIB-prepared NCM 900505 cathode charged after 100 cycles at 4.5 V: (a) mosaic bright-field STEM image, (b) dark-field STEM image, (c-d) conventional TEM ima ges of the fractured primary particles.

suggesting that the layered structure is nearly destroyed into randomly oriented nanoscale crystalline domains.

Surface Degradation. To further understand the mechanism behind the capacity fade of NCM 900505, the cycled cathode particle surfaces were examined with TEM without the usual thinning process to preserve the damaged surface structure (Figure 6). A high-resolution image of the NCM 622 surface charged to 4.3 V taken in the [100] zone at the particle edge (Figure 6a) reveals a thin layer of rock salt NiO-like structure (verified by the Fourier filtered image in the inset) as previously observed in the cycled NCA and NCM cathodes.[8,10] This NiO-layer is confined to a thickness of ~ 3 nm all along the particle surface. Raising the cutoff voltage to 4.5 V hardly affected the surface structure of the NCM 622 cathode, which is reasonable since the capacity retention for the NCM 622 cathode decreased only slightly at 4.5 V after 100 cycles; the damaged surface layer at 4.5 V is also limited to a thickness of 3 nm and the layered structure was well preserved in the particle interior (Figure 6b).

On the contrary, the surface damage is noticeably more extensive in the case of the NCM 900505 cathode cycled at 4.3 V, and the thickness of the NiO-like layer is increased to ~ 5 nm capped by a thin layer of amorphous material as shown in Figure 6c. It appears that the parasitic reaction with the electrolyte partially converted the NiO-like layer into an amorphous state through oxygen release from the layered lattice[19,32,33] and subsequently destroyed the crystal structure. TEM observation of the cycled electrodes reveal that the rock salt structure generation is exacerbated in the NCM 900505 cathode due to the higher concentration of the thermodynamically unstable Ni^{4+} on the surface. In addition, the distortion of the damaged layer was severe enough to generate polycrystalline domains (insipient stage for crystal-break up) as evidenced by a stretching of the diffraction spots corresponding to the rock salt structure into a series of arcs (comparison of Fourier transform images of the region I and the particle interior in Figure 6c). As for the NCM 900505 cathode cycled at 4.5 V, a high-resolution image from a fracture particle shown in Figure 6d indicates that a thicker layer of amorphous material (see Fourier transform of the surface region II in Figure 6d) is also present on the particle surface. It should be noted that the different extent of the surface damages incurred in the NCM 622 and NCM 900505 cathodes were apparent only when examined as is. When a thin section was prepared by FIB, the coating and etching necessary for the sample preparation wiped out the surface damage from cycling; in fact, both particle surfaces from the cycled NCM622 and NCM900505 appeared similar in the FIB-prepared samples. Indeed, the formation of thicker layer on the

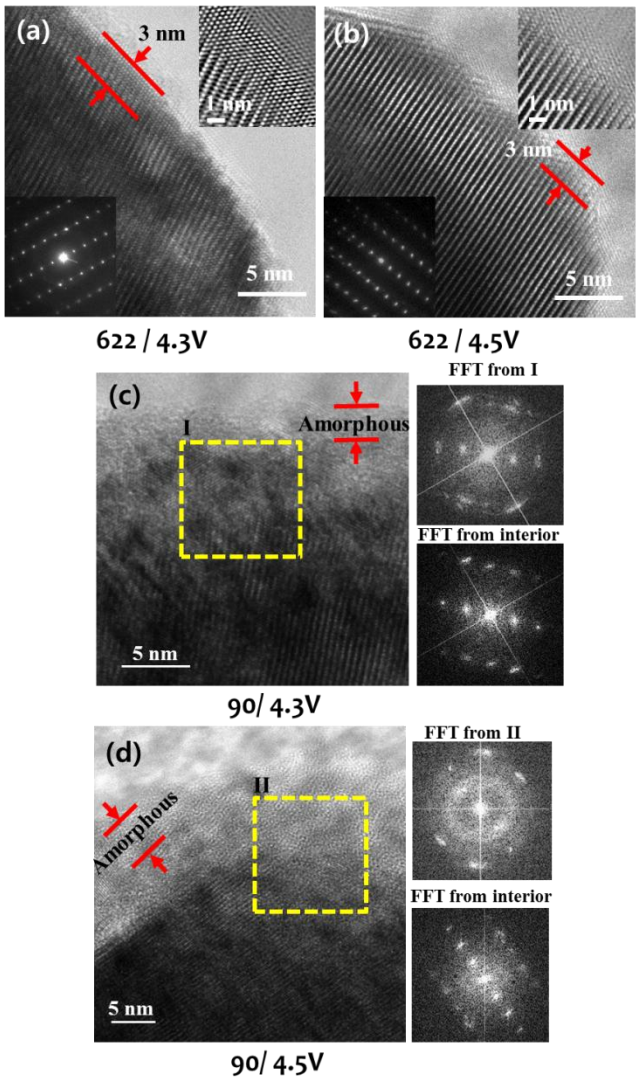

Figure 6. TEM surface images and Fourier Transform (after 100 cycles) from unprocessed electrodes of (a) NCM 622 charged to 4.3 V, (b) NCM 622 charged to 4.5 V, (c) NCM 900505 charged to 4.3 V, and (d) NCM 900505 charged to 4.5 V.

cathode of thicker impurity layer on the cathode surface increased the cell resistance as indicated by the impedance spectroscopy measurements taken at 25 ºC in the charged state of 4.3 V after the 1st, 25th, 50th, 75th, and 100th cycles (Figure S4). The Nyquist plots of the two NCM cathodes reveal that while the charge-transfer resistance (R_{ct}) of NCM 622 remains relatively unchanged during cycling, that of NCM 900505 steadily increases with increasing cycle number, i.e., the R_{ct} value increased from 5.4 Ω at the 1st cycle to 22.8 Ω by the 100th cycle for NCM 900505 cathode due to formation of the NiO-like layer on the cathode surface.

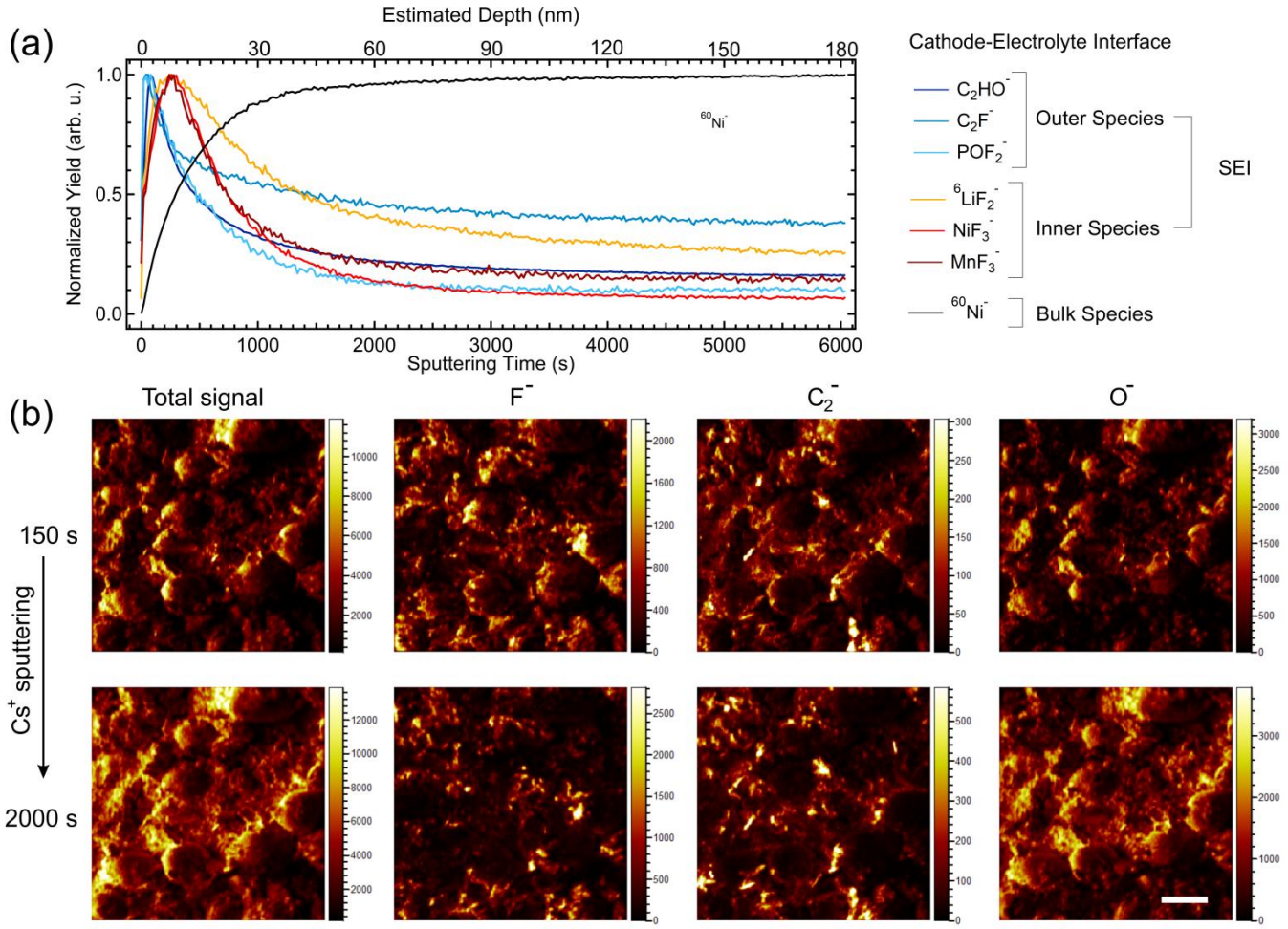

Figure 7. (a) Depth profiling of the NCM 900505 electrode cycled up to 100 cycles with a cutoff voltage of 4.3 V. The cathode-electrolyte interphase (CEI) contains multiple layers, among which an outer (passivation) and inner (dissolution) layer can be identified. (b) High resolution TOF-SIMS maps demonstrating the localization of the outer CEI species at the surface of the active material particles.

From a chemical perspective, the higher Ni content NCM also suffers from metal dissolution by HF attack. Figure S5 shows the electrolyte dissolution test, which shows that the Ni dissolution from NCM 900505 is an order of magnitude higher than that from NCM 622 by the end of the 10th day and this difference is further amplified by the end of the 20th day. Interestingly, even though NCM 900505 has one-fourth the amount of Co and Mn as NCM 622, the former showed 50 % more Co and Mn dissolution by the end of the 20th day, which may be due to a greater exposure of the Co and Mn to liquid electrolyte caused by microcrack formation within the particles.

Surface Chemical Composition. Time-of-flight secondary-ion mass spectrometry was employed to identify and locate the chemical species composing the surface (that is, the cathode-electrolyte interphase, CEI). ToF-SIMS depth profiling of the NCM 900505 cathode after cycling with a cutoff voltage of 4.3 V showed that the CEI consisted of multiple layers, among which an outer and an inner layer stands out (Figure 7a). Often, the outer layer is considered a protective layer, containing organic and inorganic species such as C_2HO^-, C_2F^-, and POF_2^-. In contrast, the inner layer is commonly associated with the dissolution of active material, in this case containing Li, Ni and Mn fluorinated species, such as $^6LiF_2^-$, NiF_3^-, and MnF_3, resulting from HF attack among other electrolyte-cathode side reactions.[34] To demonstrate the localization of the outer species on the NCM 900505 particles, comparative high-resolution maps after 150 s and 2000 s of Cs^+ sputtering was acquired as seen in Figure 7b. As illustrated, F^- and C_2^-, representing the outer CEI layer, clearly vanished from the surface of the particles after 2000 s of Cs^+ sputtering (equivalent to the removal of ~ 60 nm). On the other hand, the O^- signal, representing the oxide bulk of the particles, appeared enhanced at the particles surface, indicating the removal of the CEI. Of note, some of the electrolyte reaction species were still present in the bulk due to the electrolyte penetrating into the bulk through generated microcracks. The result is a formation of a multi-layered complex[34] covering the particle surface as outlined by the ToF-SIMS depth profiling of Figure 7a.

Thermal Stability. With such a vulnerability in the bulk and surface structure, it is not surprising that the thermal stability of NCM 900505 cathode is also poor compared to that of NCM 622 as portrayed by the differential scanning profiles in Figure 8. At a cutoff voltage of 4.3 V, the NCM 622 cathode exhibits the exothermic peak at 272 °C with a heat generation of 760 J g^{-1} while NCM 900505 exhibits the peak at a much lower temperature of 201 °C with a higher heat generation of 1,670 J g^{-1}.

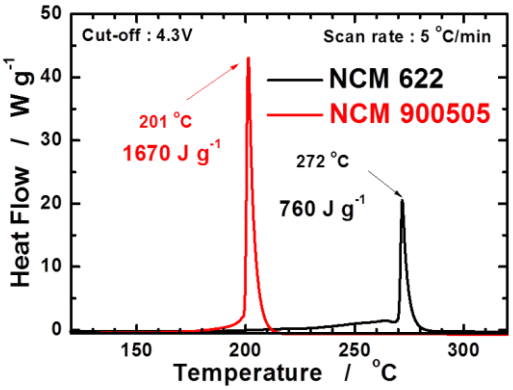

Figure 8. DSC profiles of NCM 622 (black) and NCM 900505 (red) after charging to 4.3 V.

4. Conclusion

The $Li[Ni_{0.90}Co_{0.05}Mn_{0.05}]O_2$ cathode delivers an outstanding discharge capacity of 227 mA h g^{-1} compared to $Li[Ni_{0.6}Co_{0.2}Mn_{0.2}]O_2$ (189 mA h g^{-1}) when cycled at 2.7 to 4.3 V vs. Li^o/Li^+ at 0.1C rat; it exceeds the necessary energy density suggested by DOE on the cathode level for electric vehicles. This high capacity can be ascribed to the high Ni content, which makes it characteristically similar to $LiNiO_2$, but also makes it susceptible to rapid capacity fade during cycling. A systematic investigation of the capacity fade of $Li[Ni_{0.90}Co_{0.05}Mn_{0.05}]O_2$ with dQ dV^{-1} profiles and particle cross-sectional TEM images clearly demonstrates that the poor cycle retention is largely due to the anisotropic volume change and subsequent microcrack propagation in the bulk and NiO rock salt impurity generation on the particle surface, which are exacerbated as the charge cutoff voltage increases. Such structural damages are further manifested in the EIS results and thermal stability of the cathode. As such, $Li[Ni_{0.90}Co_{0.05}Mn_{0.05}]O_2$ is an exceptional cathode material in terms of discharge capacity and rate capability but suffers from rapid capacity fade. Future efforts with cationic doping and surface protection by coating of the cathode or development of alternative electrolytes to realize a better cathode-electrolyte interface could help improve the cycle life of NCM cathodes with high Ni contents.

ASSOCIATED CONTENT

SUPPORTING INFORMATION

Rietveld refinement table. dQ dV^{-1} curves of NCM 622 and NCM 900505. *Ex-situ* XRD patterns collected with cutoff-voltages of 4.1 to 4.3 V. *Ex-situ* XRD patterns of the cathode cycled to 100 cycles. Lattice parameter changes. Nyquist plots. Metal dissolution data. This material is available free of charge via the Internet at http://pubs.acs.org.

AUTHOR INFORMATION

Corresponding Author

*E-mail: rmanth@mail.utexas.edu

Notes

The authors declare no competing financial interest.

ACKNOWLEDGMENT

The authors gratefully acknowledge the support from the Assistant Secretary for Energy Efficiency and Renewable Energy, Office of Vehicle Technologies of the U.S. Department of Energy through the Advanced Battery Research (BMR) Program (Battery500 Consortium) award number DE-EE0007762 and the Welch Foundation grant F-1254. The authors thank Professors Yang-Kook Sun and Chong Yoon at Hanyang University for, respectively, providing the hydroxide precursors for the NCM 622 and NCM 900505 samples and the assistance with the TEM.

References

(1) Mizushima, K.; Jones, P. C.; Wiseman, P. J.; Goodenough, J. B. LixCoO2 (0 < x < 1): A New Cathode Material for Batteries of High Energy Density. *Mater. Res. Bull.* **1980**, *15*, 783–789.

(2) Chebiam, R.; Kannan, A.; Prado, F.; Manthiram, A. Comparison of the Chemical Stability of the High Energy Density Cathodes of Lithium-Ion Batteries. *Electrochem. commun.* **2001**, *3*, 624–627.

(3) Gummow, R.; Thackeray, M.; David, W.; Hull, S. Structure and Electrochemistry of Lithium Cobalt Oxide Synthesised at 400 °C. *Mater. Res. Bull.* **1992**, *27*, 327–337.

(4) Ohzuku, T.; Ueda, A.; Nagayama, M, Electrochemistry and Structural Chemistry of LiNiO2 (R3m) for 4 Volt Secondary Lithium Cells. *J. Electrochem. Soc.* **1993**, *140*, 1862-1870.

(5) Arai, H.; Okada, S.; Ohtsuka, H.; Ichimura, M.; Yamaki, J. Characterization and Cathode Performance of $Li_{1-x}Ni_{1+x}O_2$ Prepared with the Excess Lithium Method. *Solid State Ionics* **1995**, *80*, 261–269.

(6) Hirano, A.; Kanno, R.;, Kawamoto, Y.; Takeda, Y.; Yamaura, K.; Takano, M.; Ohyama, K.; Ohashi, M.; Yamaguchi, Y. C Relationship between Non-Stoichiometry and Physical Properties in $LiNiO_2$. Solid State Ionics **1995**, *78*, 123-131.

(7) Yamada, S.; Fujiwara, M. . K.; M. Synthesis and Properties of $LiNiO_2$ as Cathode Material for Secondary Batteries. *J. Power Sources* **1995**, *54*, 209–213.

(8) Abraham, D. P.; Twesten, R. D.; Balasubramanian, M.; Petrov, I.; McBreen, J.; Amine, K. Surface Changes on $LiNi_{0.8}Co_{0.2}O_2$ Particles during Testing of High-Power Lithium-Ion Cells. *Electrochem. commun.* **2002**, *4*, 620–625.

(9) Lee, J. H.; Yoon, C. S.; Hwang, J.-Y.; Kim, S.-J.; Maglia, F.;

Lamp, P.; Myung, S.-T.; Sun, Y.-K. High-Energy-Density Lithium-Ion Battery Using a Carbon-nanotube–Si Composite Anode and a Compositionally Graded $Li[Ni_{0.85}Co_{0.05}Mn_{0.10}]O_2$ Cathode. *Energy Environ. Sci.* **2016**, *9*, 2152–2158.

(10) Watanabe, S.; Kinoshita, M.; Hosokawa, T.; Morigaki, K.; Nakura, K. Capacity Fading of $LiAl_yNi_{1-x-y}Co_xO_2$ Cathode for Lithium-Ion Batteries during Accelerated Calendar and Cycle Life Tests (Effect of Depth of Discharge in Charge-Discharge Cycling on the Suppression of the Micro-Crack Generation of $LiAl_yNi_{1-x-y}Co_xO_2$ Particle. *J. Power Sources* **2014**, *260*, 50–56.

(11) Zheng, S.; Huang, R.; Makimura, Y.; Ukyo, Y.; Fisher, C. A. J.; Hirayama, T.; Ikuhara, Y. Microstructural Changes in $LiNi_{0.8}Co_{0.15}Al_{0.05}O_2$ Positive Electrode Material during the First Cycle. *J. Electrochem. Soc.* **2011**, *158c*, A357-A362.

(12) Yoon, C. S.; Jun, D.-W.; Myung, S.-T.; Sun, Y.-K. Structural Stability of $LiNiO_2$ Cycled above 4.2 V. *ACS Energy Lett.* **2017**, *2*, 1150–1155.

(13) Kim, U. H.; Lee, E. J.; Yoon, C. S.; Myung, S. T.; Sun, Y. K. Compositionally Graded Cathode Material with Long-Term Cycling Stability for Electric Vehicles Application. *Adv. Energy Mater.* **2016**, *6*, 1601417.

(14) Lim, J.-M.; Hwang, T.; Kim, D.; Park, M.-S.; Cho, K.; Cho. M. Intrinsic Origins of Crack Generation in Ni-rich LiNio.8C00.1Mno.1O2 Layered Oxide Cathode Material Sci. Rep., **2017**, 7, 39669.

(15) Shaju, K. M.; Subba Rao, G. V.; Chowdari, B. V. R. Performance of Layered $Li(Ni_{1/3}Co_{1/3}Mn_{1/3})O2$ as Cathode for Li-Ion Batteries. *Electrochim. Acta* **2002**, *48*, 145–151.

(16) Park, S.-H.; Shin, H.-S.; Myung, S.-T.; Yoon, C. S.; Amine, K.; Sun, Y.-K. Synthesis of Nanostructured $Li[Ni_{1/3}Co_{1/3}Mn_{1/3}]O_2$ via a Modified Carbonate Process. *Chem. Mater.* **2005**, *17*, 6–8.

(17) U.S. Department of Energy. Energy Storage 2015 Annual Report. **2016**, 1-263.

(18) Andre, D.; Kim, S.-J.; Lamp, P.; Lux, S. F.; Maglia, F.; Paschos, O.; Stiaszny, B. Future Generations of Cathode Materials: An Automotive Industry Perspective. *J. Mater. Chem. A* **2015**, *3*, 6709–6732.

(19) Noh, H. J.; Youn, S.; Yoon, C. S.; Sun, Y. K. Comparison of the Structural and Electrochemical Properties of Layered $Li[Ni_xCo_yMn_z]O_2$ (X = 1/3, 0.5, 0.6, 0.7, 0.8 and 0.85) Cathode Material for Lithium-Ion Batteries. *J. Power Sources* **2013**, *233*, 121–130.

(20) Park, S. H.; Yoon, C. S.; Kang, S. G.; Kim, H.-S.; Moon, S.-I.; Sun, Y.-K. Synthesis and Structural Characterization of Layered $Li[Ni_{1/3}Co_{1/3}Mn_{1/3}]O2$ Cathode Materials by Ultrasonic Spray Pyrolysis Method. *Electrochim. Acta* **2004**, *49*, 557–563.

(21) Li, W.; Song, B.; Manthiram, A. High-Voltage Positive Electrode Materials for Lithium-Ion Batteries. *Chem. Soc. Rev.* **2017**, *46*, 3006–3059.

(22) Augustyn, V.; Manthiram, A. Effects of Chemical versus Electrochemical Delithiation on the Oxygen Evolution Reaction Activity of Nickel-Rich Layered $LiMO_2$. *J. Phys. Chem. Lett.* **2015**, *6*, 3787–3791.

(23) Yoon, C. S.; Choi, M. H.; Lim, B.-B.; Lee, E.-J.; Sun, Y.-K. Review—High-Capacity $Li[Ni_{1-x}Co_{x/2}Mn_{x/2}]O_2$ (X = 0.1, 0.05, 0) Cathodes for Next-Generation Li-Ion Battery. *J. Electrochem. Soc.* **2015**, *162*, A2483–A2489.

(24) Kim, M. H.; Shin, H. S.; Shin, D.; Sun, Y. K. Synthesis and Electrochemical Properties of $Li[Ni_{0.8}Co_{0.1}Mn_{0.1}]O2$ and $Li[Ni_{0.8}Co_{0.2}]O_2$ via Co-Precipitation. *J. Power Sources* **2006**, *159*, 1328–1333.

(25) Wu, F.; Tian, J.; Su, Y.; Wang, J.; Zhang, C.; Bao, L.; He, T.:; Li, J.; Chen, S. Effect of Ni^{2+} Content on Lithium/Nickel Disorder for Ni-Rich Cathode Materials. *ACS App. & Mater. Interfaces* **2015**, 7, 7702–7708.

(26) Myung, S.-T.; Noh, H.-J.; Yoon, S.-J.; Lee, E.-J.; Sun, Y.-K. Progress in High-Capacity Core–Shell Cathode Materials for Rechargeable Lithium Batteries. *J. Phys. Chem. Lett.* **2014**, *5*, 671–679.

(27) Zheng, J.; Kan, W. H.; Manthiram, A. Role of Mn Content on the Electrochemical Properties of Nickel-Rich Layered $LiNi_{0.8-x}Co_{0.1}Mn_{0.1+x}O_2$ ($0.0 \leq x \leq 0.08$) Cathodes for Lithium-Ion Batteries. *ACS Appl. Mater. Interfaces* **2015**, *7*, 6926–6934.

(28) Cabana, J.; Monconduit, L.; Larcher, D.; Palacín, M. R. Beyond Intercalation-Based Li-Ion Batteries: The State of the Art and Challenges of Electrode Materials Reacting through Conversion Reactions. *Adv. Mater.* **2010**, *22*, 170–192.

(29) Li, W.; Reimers, J.; Dahn, J. In Situ X-Ray Diffraction and Electrochemical Studies of $Li_{1-x}NiO_2$. *Solid State Ionics* **1993**, *67*, 123–130.

(30) Kondrakov, A. O.; Schmidt, A.; Xu, J.; Geβwein, H.; Mönig, R.; Hartmann, P.; Sommer, H.; Brezesinski, T.; Janek, J. Anisotropic Lattice Strain and Mechanical Degradation of High- and Low-Nickel NCM Cathode Materials for Li-Ion Batteries. *J. Phys. Chem. C* **2017**, *121*, 3286–3294.

(31) Miller, D. J.; Proff, C.; Wen, J. G.; Abraham, D. P.; Bareño, J. Observation of Microstructural Evolution in Li Battery Cathode Oxide Particles by in Situ Electron Microscopy. *Adv. Energy Mater.* **2013**, *3*, 1098–1103.

(32) Konishi, H.; Yuasa, T.; Yoshikawa, M. Thermal Stability of $Li_{1-y}Ni_xMn_{(1-x)/2}Co_{(1-x)/2}O_2$ Layer-Structured Cathode Materials Used in Li-Ion Batteries. *J. Power Sources* **2011**, *196*, 6884–6888.

(33) Venkatraman, S.; Shin, Y.; Manthiram, A. Phase Relationships and Structural and Chemical Stabilities of Charged $Li_{1-x}CoO_{2-\delta}$] and $Li_{1-x}Ni_{0.85}Co_{0.15}O_{2-\delta}$] Cathodes. *Electrochem. Solid-State Lett.* **2003**, *6*, A9-A12.

(34) Li, W.; Dolocan, A.; Oh, P.; Celio, H.; Park, S.; Cho, J.; Manthiram, A. Dynamic Behavior of Interphases and its Implication on High-energy-density Cathode Materials in Lithium-ion Batteries. *Nat. Commun.* **2017**, *8*, 14589.

Table of Contents